Inference of Granger-causal relations in molecular systems — a case study of the functional hierarchy among actin regulators in lamellipodia

Jungsik Noh[1], Tadamoto Isogai[1], Joseph Chi, Kushal Bhatt and Gaudenz Danuser[2]

Lyda Hill Department of Bioinformatics, UT Southwestern Medical Center, Dallas, TX 75390, USA

[1] These authors contributed equally

[2] Correspondence: Gaudenz.Danuser@UTSouthwestern.edu

Abstract

Many cell regulatory systems implicate significant nonlinearity and redundancy among components. The regulatory network governing the formation of lamellipodial and lamellar actin structures is prototypical of such a system, containing tens of actin-nucleating and -modulating molecules with strong functional overlap. Due to instantaneous compensation, the strategy of phenotyping the system response to perturbation of individual components provides limited information on the roles the targeted component plays in the unperturbed system. Accordingly, despite the very rich data on lamellipoidial actin assembly, we have an incomplete understanding of how individual actin regulators contribute to lamellipodial dynamics. Here, we present a case study of perturbation-free reconstruction of cause-effect relations among actin regulators, applying the framework of Granger-causal inference to constitutive image fluctuations that indicate regulator recruitment and dissociation. Our analysis defines distinct active zones for actin regulators within the lamellipodia and lamella and establishes actin-dependent and actin-independent causal relations with actin filament assembly and edge motion. We demonstrate the specificity and sensitivity of the analysis and propose that edge motion is driven by assembly of two independently operating actin filament structures.

Introduction

Many cell functions are governed by complex biochemical and biophysical regulatory circuits with functional overlaps – or redundancy – among components, as well as feed-back and feed-forward interactions. This represents a major challenge in the study of component functions. The dogma in the field prescribes that ‘mechanism’ of cellular regulation ought to be deduced by phenotyping under component perturbation. However, in the face of redundancy and nonlinearity phenotypes are strictly uninterpretable with respect to the function of the perturbed component (1, 2). Phenotypes show how the circuit adapts to the perturbation, which is generally not equivalent to the function the targeted component assumes in the unperturbed circuit. Of note, the disconnection between phenotype and component function is intrinsic to the nonlinearity and redundancy of the circuit and does not relate to the widely-discussed additional complication of genetic and proteolytic cellular adaptation to long-term perturbation (3). To dissect cellular regulation the field needs novel approaches that overcome the limitations of probing by perturbation.

A prototypical case of a complex regulatory circuit is the machinery driving the formation of lamellipodia and lamella actin networks (4, 5). In migrating cells, lamellipodia form as part of the leading edge. In non-polarized cells lamellipodia-like structures emerge in the form of surface ruffles serving as mechanical and chemical probes of the surrounding and as modulators of the subcellular organization of molecular signals (6). Lamellipodia formation is driven by the assembly of a dynamic filamentous actin (F-actin) network. The dynamics of network assembly is controlled by dozens of actin-binding proteins with distinct structural and kinetic properties (4, 7-9). The complexity in architectural dynamics is superimposed by the complexity of biochemical signal, which orchestrate F-actin dynamics via branching, elongation, capping, and severing in response to cell-intrinsic and -extrinsic mechanical and chemical cues. (Figure 1A). Although genetic and molecular perturbation have been instrumental in compiling an inventory of the system components and their basic contributions to the lamellipodia formation process, dissection of the functional hierarchy between the various component processes has remained elusive. Perturbation of any component almost instantaneously rebalances the stoichiometry and configuration of interactions among the diverse actin regulators (5).

Live cell fluorescence imaging combined with computer vision algorithms emerged as a perturbation-conscientious complementary approach designed to study molecular pathways embedded in actin regulatory networks (2, 5, 10-14). Molecular activities, including fluorescence intensity fluctuations and spatial recruitment profiles of e.g., actin modulators, were extracted from live cell movies to study their association with the F-actin network during protrusion/retraction events. Fluctuation time series were then exploited to establish the spatiotemporal coordination among the molecular and morphodynamic activities, assuming that the numerical coupling of the two is an indicator of local functional relations (10, 11, 13-17). This paradigm has also been applied to the analysis of regulatory signals upstream of actin dynamics (18-21). However, these analyses do not inform on the causal relation between activities.

Given a set of temporally resolved variables, the hierarchy of cause-and-effect relations can be inferred by statistical assessment of the power of the signal of a putative cause for the prediction of the signal of a putative effector (Figure 1B). This analysis is distinct from a correlation analysis, which merely infers the level of co-fluctuations between two variables. Two variables without causal coupling may be highly correlated because of a common input (Figure 1B). The notion of inferring causality based on the prediction power of one

variable for another has long been employed in econometrics and neurophysiology (22, 23). The most popular of these frameworks is the Granger-causality (GC) analysis, which defines a statistical test of the hypothesis that past observations of one variable possess indispensable information for explaining the current and future observations of a second variable (24). Because of the explicit temporal direction in the relationships, the GC framework also permits analysis of nonlinear regulatory motifs such as feedback, redundant pathways, and even nested feedbacks (Figures 1C-1E). These are common sources of complexity in molecular systems such as the lamellepodial F-actin network.

Granger-causal (G-causal) relations must be interpreted only within the system of observable variables. For example, if the observed signal of a variable X is causative for an unobserved latent factor that is causative for the observed signal of a variable Y, then X will be determined as G-causal for Y (Figure 1F). While in many biological studies, knowledge of such indirect relations can yield great insight for practical purposes, the prediction of G-causal relation is not to be mistaken for a causality that pinpoints direct molecular interactions. Accordingly, we refer to G-causal relations in regulatory networks as functional causality. In contrast, the prediction of Granger-noncausality has the strong implication that the two considered variables are independent, regardless of any latent factor (Figure 1G). This property permits the exclusion of functional relations at the level of the whole system based on a partially observed system (25).

In this work, we illustrate GC analysis of lamellipodial F-actin regulation. Using multivariate time-series representing the spatiotemporal molecular and cell morphological dynamics of the system, we build generative stochastic models that capture the information within the system. Our GC analytical pipeline, for example, shows that actin dynamics at the most proximal zone, i.e. ~0–0.7 μm from the cell edge Granger-causes (G-causes) edge motion, while actin more distal from the cell edge (zones ~0.7–1.4 μm) is predicted as Granger-noncausal (G-noncausal) for edge motion. Notably, this latter zone showed a strong positive correlation between F-actin dynamics and edge motion, demonstrating that GC analysis is distinct from correlation: Correlation is not causation. We further applied the GC pipeline to identify the causal relations between actin modulators and F-actin dynamics. For Arp2/3 and VASP, for example, our analysis determines that both modulators G-cause edge motion yet operate independently from each other in distinct pathways. This suggests that at least two structurally, molecularly and kinetically distinct actin networks exist to coordinate

edge motion – a conclusion that is inaccessible by conventional perturbation and correlation-dependent approaches.

Results

Workflow of Granger-causal pathway inference between regulators of lamellipodial actin dynamics

To study Granger-causal relationships between actin regulators during lamellipodia dynamics, we required time series of their recruitment profiles as the cell underwent spontaneous events of protrusion and retraction. We accomplished this by fluorescently tagging actin regulators at very low concentration or endogenously, so as to not perturb the endogenous stoichiometry among regulators, followed by imaging their intensity fluctuations over time (Figure 2(i)). Importantly, by ensuring very low expression of the labelled regulator, local intensity changes largely reflect the specific association of regulator with F-actin (26). We illustrate the workflow of time series extraction and analysis with Arp2/3 as the test case. We endogenously tagged Arp3 with HaloTag (Halo) using CRISPR/Cas9 in U2OS cells, and co-imaged Arp3-Halo^{CR} in the presence of very low levels of mNeonGreen-tagged actin expressed under a truncated CMV promoter. Cycles of edge protrusion and retraction events were sampled every 3 seconds for 15 minutes. Visual inspection of these cycles in conjunction with the F-actin dynamics revealed the well-established characteristics of a lamellipodium with actin treadmilling at the cell front and a lamella with slower and spatially less coherent actin dynamics beneath (15) (Video S1).

To capture fluctuation time series of edge motion and underlying cytoskeletal dynamics, we partitioned the protruding and retracting front of the cell into submicron-scale probing windows, and tracked their positions over time so that they maintained a constant relation with an edge sector of the same submicron scale, as described previously (18, 27). This generates a coordinate system that allows simultaneous registration of spatiotemporal fluorescent intensity fluctuations and cell edge protrusion/retraction dynamics (Figure 2(ii), Video S2-S3). The size of the probing windows was fine-tuned to be several-fold smaller than the average length scale of protrusion and retraction events, and small enough to capture the distinct cytoskeleton dynamics in lamellipodium and lamella. Specifically, the lamellipodia depth in the U2OS cells measured 1.4 µm, on average. Thus, for our spatial analyses, we defined the lamellipodia region as the band ~0–1.4 µm

from the cell edge and the lamella region as the band ~1.4–2.9 μm from the cell edge. We further divided these regions into half to examine potential spatial gradients in Arp2/3 and actin activities within each region. For each probing window we then read out time series of locally averaged Arp2/3 and actin intensities and mapped them into space-time matrices, which conveniently display the cyclic dynamics of Arp2/3 recruitment and F-actin assembly (Figure 2(iii), See Methods). For the window row at the cell front, we also read out the average velocity, with positive and negative values indicating protrusion and retraction, respectively. Of note, any probing window in layer 2 and higher is unambiguously associated with one probing window in layer 1. This permits the analysis of causal relations between different types of events, e.g. Arp2/3 and velocity, or Arp2/3 and another actin regulator, in the same or different window layers.

To illustrate the inference of GC relations we focus first on the questions 'how causal' Arp2/3 recruitment to a particular target window is for the assembly of actin in the same window, and 'how causal' this F-actin response is for cell edge motion at that location. Per Granger's definition (22), Arp2/3 recruitment is Granger-causal (G-causal) for actin, if the Arp2/3 recruitment profile is indispensable for predicting the assembly of F-actin in the same window. The focused assembly of F-actin in a window is predicted based on a multi-dimensional stochastic model that accounts for the past recruitment profiles of both F-actin and Arp2/3 in the target window as well as the surrounding windows. The model also includes the protrusion/retraction (P/R) velocities of the adjacent edge segments as potentially predictive variables for the Arp2/3–F-actin relation (Figure 1(iv), See Methods). The indispensability of Arp2/3 recruitment for F-actin assembly at a given location is statistically tested by comparing two prediction models: 1) the full model incorporating fluctuation time series of Arp2/3, F-actin and associated edge motion in the target window and the four neighboring windows, and 2) the reduced model equivalent to the full model minus the Arp2/3 fluctuation time series in the target window (Figure 2(iv)). If the Arp2/3 fluctuation series in the target window is indispensable to explain F-actin assembly, the full model will lead to a significantly better prediction performance than the reduced model. Of note, because of the additional degrees of freedom, the full model will always exhibit better prediction performance than the reduced model, as assessed by variance of the difference between predicted and measured F-actin fluctuations. The key question is whether the additional degrees of freedom *significantly* improve the prediction performance. This question is answered by application of a Fisher test on the ratio between the variances

under the null-hypothesis that this ratio assumes values close to 1, i.e. full model and reduced model are equally strong predictors (Figure 2(iv)). In the example of Figure 2, low P-values, therefore, indicate a causal link between Arp2/3 recruitment and F-actin assembly.

The subcellular GC relations distinguish direct from indirect causal interactions. For example, if a pathway entails a linear chain of biochemical interactions A → B → C, then A is referred to as directly causal for B, and indirectly causal for C. In Figure 2, Arp2/3 recruitment is determined to G-cause F-actin assembly. This GC relation is direct and cannot be mediated by any other observed variable, i.e. edge motion. If the pathway were to consist of a chain Arp2/3 → edge motion → actin, then the Arp2/3 recruitment would have been dispensable in predicting F-actin assembly, i.e. the edge motion would have accounted for the actin assembly.

To draw firm and reproducible statistical conclusions on the causality between variables, we integrated the subcellular P-values of the GC tests for multiple independent cells. To achieve this, our pipeline tests whether the subcellular G-causal evidences appear consistently over multiple cells in independent experiments. From a statistical perspective, the *sampling unit*, i.e. the physical entity that is repeatedly measured independent from any other entity, is one cell. Since a statistical conclusion is a statement about a population of sampling units hypotheses need to be tested based on per-cell measurements, accounting for cell-to-cell variability as the main source of random variation. To accomplish this, we computed the median of P-values of GC evidences over many probing windows as the per-cell measurement. A per-cell median P-value of less than 0.05 indicates that the majority of the subcellular windows in the cell shows GC-causal interactions between the investigated variables (Figure 2(v)). Then, we test whether the per-cell median P-values of *n* cells are significantly smaller than the threshold 0.05, using the one-sample signed rank test. If the rank test determines that a GC relationship consistently appears in the majority of windows over independently imaged cells, we conclude that the two tested variables are causally connected (Figure 2(vi)).

After completing the pairwise testing of GC relationships between all variables among the observed system, causal relations are integrated and represented as a graph with variable interactions (28) (Figure 2(vii)). Of note, these Granger-causality graphs may identify feedback interactions between variables. To account for spatial variation in causal interactions, we compute graphs separately for lamellipodia and lamella

(in our U2OS cell model 0–0.7 µm and 0.7–1.4 µm vs 1.4–2.2 µm and 2.2–2.9 µm, respectively). For the specific variables Arp2/3, F-actin, and edge velocity, the graphs indicate a causal interaction between Arp2/3 and actin, as expected, as well as a feedback from F-actin to Arp2/3. This feedback may be explained by the intrinsic recruitment dynamics of the dendritic polymer network, in which the nucleation of branches yields additional filaments that in turn can be branched again. Actin is also in a causal feedback relation with edge velocity, however only for the probing windows in layer 0–0.7 µm. This indicates that the actin dynamics at greater distances from the cell edge does not cause edge motion, and that edge velocity feeds back onto F-actin assembly in the first layer of probing windows. Whereas the forward link from actin to movement relates to the conversion of actin filament growth into mechanical push of the cell edge through mechanisms such as the Brownian Ratchet (29), the feedback may be governed by several mechanisms including mechanical and chemical force-feedback from the increasing membrane tension or membrane deformation (10, 30-33). Importantly, the graphs indicate that there is no direct causal interaction between Arp2/3 and velocity. In forward direction this means that any modulation in Arp2/3 recruitment translates into modulation of edge velocity only via F-actin dynamics. The absence of a causal link in reverse direction implies that the predicted feedback from edge motion to actin in windows in layer 0–0.7 µm is independent of Arp2/3, i.e. signals must exist that translate the morphological dynamics or variation in mechanical forces into actin nucleators other than Arp2/3. For example, this data refutes the model that bending of actin filaments pressing against the plasma membrane contributes significantly to an increased Arp2/3 recruitment (34). These first results demonstrate the power of Granger-causality analyses to functionally relate molecular processes in a hierarchical and nonlinear order.

Actin and Arp2/3 fluctuations correlate with edge velocity

To highlight the difference between G-causal relations and correlative relations, we focus on the cross-correlations (CCs) between the same three variables Arp2/3, F-actin, and edge velocity. For both GC analysis and correlation analysis it is essential that the time scales of fluctuations match between variables. A straightforward approach to determine the time scale of stochastic time series is the auto-correlation function (ACF). The ACF of edge velocities averaged over ~100 windows per cell and integrated over 10 cells,

displayed a characteristic main lobe with a time-lag of ~30 s for the maximal negative correlation, which corresponds to half of the dominant P/R cycle of ~60 s (Figure 3A). In stark contrast, the ACFs of F-actin and Arp2/3 displayed much longer cycles of > 4 min (Figures 3B and 3C). These cycles correspond to higher variation in baseline F-actin and Arp2/3 recruitment, visible in the space-time maps of Figure 2(iii) as broad 'smears' across all windows. Intriguingly, the strong visible correspondence between F-actin and Arp2/3 in the space-time map confirmed their co-modulation. However, because of the difference between time scales, we concluded that variations in baseline recruitments of F-actin and Arp2/3 were not related to edge motion.

Nevertheless, since Arp2/3 and F-actin dynamics are known to be related to protrusion and retraction dynamics, we hypothesized that the overall F-actin and Arp2/3 fluctuation signals ought to contain shorter time scale fluctuations that should align with that of edge motion cycles, and that this information is masked by variations in the baseline recruitment profiles. To test this, we decomposed the raw time series of F-actin and Arp2/3 recruitment into low-frequency (LF) oscillations and low-frequency subtracted (LFS) oscillations (Figures 3B-3E, see Methods). The LFS time series of both F-actin and Arp2/3 recruitment displayed the same space-time fluctuation patterns as that of edge velocity. Indeed, the ACFs of the LFS signals closely matched the ACF of edge velocities (Figures 3F and 3G). For visual validation of this result, we generated animations where the LFS-recruitment of F-actin and Arp2/3 co-fluctuated very clearly with edge movements (Video S4), whereas the low-frequency baseline recruitment appeared unrelated to the cell edge movement.

To determine the coupling between LFS-recruitment and edge motion in quantitative terms, we computed the cross-correlation (CC) between the LFS variables and edge velocity in each window as previously described (18). For both F-actin and Arp2/3, the patterns of CC with edge velocity were homogeneous across the subcellular windows in the same layer, whereas it differed in between layers (Figures 3H and 3I). We averaged the CC over the windows in each layer for each cell. The per-cell averaged CC curves as a function of time-lag were remarkably consistent over many cells (n = 20), indicating preserved mechanisms of coordinated recruitments of F-actin and Arp2/3 during the P/R cycles (Figures 3J and 3K). Within the entire lamellipodia area (layers 1 and 2; ~0–1.4 μm), the fluctuations of F-actin assembly best correlated with the edge velocity with a time delay of ~9 s (Figure 3J), which is in line with previous reports of correlative relations between actin recruitment and edge movement in epithelial cells (13, 14). In contrast,

Arp2/3 recruitment displayed a differential correlation pattern at the front (layer 1) and back (layer 2) of the lamellipodia. In layer 1, Arp2/3 fluctuations preceded edge velocity fluctuations by ~3 s, whereas in layer 2, the Arp2/3 fluctuations followed the edge velocity by ~6 s (Figure 3K).

Our correlation analysis and interpretations operate under the assumption that intensity fluctuations in F-actin and Arp2/3 are synonymous for biochemical activity, i.e. the addition or removal of actin subunits and Arp2/3 complexes, respectively, to or from the lamellipodial network. To test the validity of this assumption, we performed correlation analyses with images of diffuse HaloTag alone. The CC curves between cytoplasmic HaloTag intensities and edge velocity consistently showed positive correlation values at negative time lags and negative correlations at positive time-lags (Figure S1A). The confidence band about these correlation curves are much wider than the confidence bands for actin and Arp2/3 correlations in the lamellipodia region (Figures 3J and 3K), consistent with the notion that the timing of fluctuations in the diffuse HaloTag signal relative to cell edge movements is much less rigid than the timing of cytoskeleton components associated with cell motility. To explain the mechanism underlying the positive and negative lobes, we had to turn to kinetic maps, which indicate the average accumulation of a fluorescent signal relative to a morphodynamic event such as protrusion or retraction onset (Figure S1B), as previously described (13, 19). The typical fluorescence intensities of the cytoplasmic HaloTag reached its highest values after the fastest retraction, which explained the negative correlations between the HaloTag and edge velocity at positive time-lags. This peak of the HaloTag mean intensity was still observable before the fastest protrusion, which was captured by the positive correlations at negative time-lags. These fluctuation patterns of cytoplasmic HaloTag depicted systematic volume changes near the edge during P/R cycles, where the volume was maximized right before the protrusion onset and minimized at or right before the retraction onset as the cell edge maximally stretched out.

The CC pattern of a diffuse, cytoplasmic HaloTag with edge velocity resembled the CC patterns of both actin and Arp2/3 with edge velocity in the most distal region we analyzed (layer 4; 2.2–2.9 µm) (Figures 3J and 3K). This suggests that in the lamella, the LFS F-actin and Arp2/3 signals reflect a fraction of fluorescent probes that are diffusing in contrast to the relatively static cytoskeleton structures in the lamella such as cortical actin fibers, whose fluorescence fluctuations are captured by the LF baseline recruitment signal. The CC patterns of F-actin and Arp2/3 recruitments with edge velocity in the transitional region 1.4–2.2 µm (layer 3)

exhibited a mixture of the lamellipodial and cytoplasmic CC curves. This shows that the CC curves of F-actin and Arp2/3 differentiate two distinct cytoskeleton behaviors in lamellipodium and lamella, and that the lamellipodium-to-lamella transition in U2OS cells locates in the 1.4–2.2 μm region.

A generative stochastic model to distinguish causation from correlation

Since cytoplasmic, biologically non-functional signals still correlated with edge velocity, correlations alone are insufficient to identify causal functions of molecules in lamellipodial dynamics. To accomplish causal inference, we had to formulate a generative, stochastic model that specifies the dependencies of the edge velocities on molecular activities in subcellular space and time. Towards such a model, we first assembled a spatially propagating autoregressive (SPAR) model that prescribes the spatial propagation of molecular activities in a target window to four adjacent windows (Figure S1C, See Methods). Analysis of actin dynamics by the SPAR model detected propagation of F-actin signal fluctuations in retrograde direction in regions with prominent actin retrograde flow, as expected (Figure 4A, Video S5). It also revealed that actin fluctuations propagate laterally throughout the entire lamellipodia. In contrast, per the SPAR model fluctuations in the cytoplasmic HaloTag signal did not spatially propagate in most lamellipodia/lamella regions (Figure 4B, Video S6). This illustrates the power of SPAR analysis to differentiate between spatiotemporally propagated and non-propagated molecular activities.

GC analysis identifies a causal chain from Arp2/3 to F-actin to edge velocity at the lamellipodia front

By extending the SPAR model, we formulated a generative stochastic model between two spatiotemporally coupled molecular activities and edge velocity (Figure 2(iv)). Applied to the analysis of lamellipodia dynamics, we first statistically tested the causal effect of Arp2/3 recruitment on F-actin assembly at each subcellular probing window in the cell shown in Figure 2(i). Most windows in the lamellipodia region (layers 1 and 2; ~0–1.4 μm) displayed significant GC P-values, whereas the Arp2/3 did not G-cause actin fluctuation in the majority of windows outside the lamellipodia (layers 3; ~1.4–2.2 μm) (Figures 4C and S2A). As one would expect, F-actin fluctuations at the lamellipodia front (layer 1) had G-causal effects on edge motion, with almost all probing windows showing P-values < 0.0001 (Figure 4D). The strong GC relation from

F-actin to motion was sharply reduced to a median P-value of 0.032 over all windows at the lamellipodia base (layer 2, Figure S2B). This demonstrates the high spatial resolution of the SPAR models in delineating spatial zones of distinct causal hierarchy among subcellular events. In agreement with the spatial gradient in causation, F-actin fluctuations at the lamellipodium-to-lamella transition and the lamella were G-noncausal for edge velocity in most windows (median P-values 0.419 and 0.571 over all windows in layers 3 and 4, respectively; Figure 4D and not shown). For the remaining combinations of pairwise relations between F-actin, Arp2/3 and edge velocity, we found distinct subcellular patterns of causality reflecting the fine-grained spatial regulation of the lamellipodial and lamellar actin machinery (Video S7-S12).

We then examined whether the patterns of G-causal relations identified in a single cell were reproducible in cells imaged over independent experimental sessions (Figure 4E). Applied to a population of n = 20 cells, these statistical analyses confirmed a causal relation from Arp2/3 to F-actin assembly in layers 1 and 2 (~0–1.4 μm) but not in layers 3 and 4. Our data also showed that F-actin assembly G-causes Arp2/3 recruitment in the lamellipodia (rank test P-values < 0.001), confirming the autocatalytic properties of Arp2/3-mediated dendritic nucleation model (35-38). Both forward and feedback causal relations between Arp2/3 and F-actin were insignificant in layers 3 and 4 (rank test P-values > 0.522, Figure 2(vii)), demonstrating that the Arp2/3-actin functional interaction involved in the fast oscillating P/R events is confined to the lamellipodia area. Similarly, the analysis of median P-values in cell cohorts supported a strong G-causal relation from F-actin to edge motion (rank test P = 0.001, Figure 4E), but no significant relation deeper into the lamellipodia (rank test P = 0.935; Figure 4E).

A critical insight gained from a SPAR model that combines Arp2/3, F-actin, and edge motion as time-resolved variables is that Arp2/3 recruitment at the lamellipodia front is not G-causal for edge velocity (rank test P = 0.135, Figure 4E). Since the GC framework identifies direct causal effects that are not mediated by other observed variables, this result describes a causal cascade Arp2/3 → F-actin → edge velocity, i.e. any causal effect from Arp2/3 recruitment to edge motion is fully mediated by F-actin assembly. Indeed, when we excluded the F-actin data from the SPAR model, the GC pipeline predicted a strong G-causal relation from Arp2/3 to edge velocity in layer 1 (rank test P < 0.001), but not in layer 2 (rank test P = 0.977, Figures S2C-

S2E). This shows that the proposed mechanism of G-causal inference distinguishes direct from indirect causal effects among the observed components of a molecular system.

Interpretation and specificity of GC relations

The change in GC topology between the two- and three-component system implied that the Arp2/3 recruitment variable is dispensable for the prediction of edge velocity under consideration of F-actin assembly fluctuations (Figures S2F-S2H and 2(vii)). This result rules out the possibility that any other variable in the system besides F-actin could be mediating the causal effect of Arp2/3 on edge velocity. If such a hidden mediator were to exist, then the GC analysis in the three-component model would predict an additional G-causal relation from Arp2/3 to edge velocity bypassing F-actin.

To further validate the specificity of GC inference, we applied the pipeline to an inert HaloTag cytoplasmic control data (n = 12 cells). As expected, the analysis determined that cytoplasmic HaloTag fluctuation is non-causal for F-actin assembly or edge velocity (Figure S3, rank test P-values > 0.633), although the fluctuations correlate with edge motion quite significantly (Figure S1A). This again underlines the ability of the presented pipeline to separate causal from correlative relation.

mDia1 recruitment G-causes F-actin assembly at the lamellipodia base and in the lamella and an actin-independent function at the lamellipodia front

Using the GC pipeline we set out to determine where other actin nucleators and modulators affect actin assembly and cell edge protrusion/retraction. We started with the formin family member mDia1. Formins are known to bind to the barbed-ends and processively elongate linear actin filaments. We stably depleted endogenous mDia1 in U2OS cells using lentiviral short hairpin RNA and introduced exogenous SNAP-tagged mDia1 and mNeonGreen-tagged actin under a truncated CMV promoter to follow their dynamics. Live cell movies displayed dynamic recruitment of mDia1 near the cell edge along with the edge protrusion/retraction cycles (Figure S4A, Video S13). Applying causal inference, we found no G-causal interactions of mDia1 with either actin or edge motion (Figures S4B and S4C). This result seemed to contradict previous reports that suggested in other cell types mDia1 may function as the initiator of actin assembly and protrusion (13, 38). We

suspected that the level of overexpression of mDia1 (Figure 5A), albeit experimentally controlled as much as possible, resulted in a significant perturbation of the stoichiometry among the nucleators, which masked mDia1's proper function. We thus inserted by CRISPR/Cas9 a SNAP-tag before mDia1's N-terminal sequence but found the resulting fluorescence movies to have too low signal-to-noise ratio (SNR) for a meaningful causality analysis (data not shown). To overcome the deficiency in SNR, we decided to endogenously tag mDia1 with a tandem mNeonGreen2-based split fluorescence protein (sFP) strategy (39) (Figure 5B), which primarily suppresses background, yet amplifies the signal.

Live cell movies of endogenous mDia1 displayed multiple spots of dynamic recruitment a few microns back from the cell edge, which were unobservable with exogenous expression of tagged mDia1 (Figure 5C). The spots co-localized with spots enriched for actin and they appeared to be associated with strongly protruding cell edge segments (Video S14).

Using CC analysis, we found that, unlike F-actin and Arp2/3, mDia1 recruitment and edge velocity correlated homogenously across the lamellipodia and lamella. The CC curves over multiple cells (n = 14) consistently showed maximal negative values at positive lags of ~3-9 s (Figure S4D). Kinetic maps indicated that this negative peak was associated with mDia1 recruitment after maximal retraction and before protrusion (Figure S4E), consistent with the previous observations (13).

To determine how much this mDia1 recruitment causes actin assembly and edge motion, we applied the GC pathway inference pipeline to mDia1/actin live cell movies. On a per-cell basis, e.g., for the cell shown in Figure 5C, most windows at the lamellipodia base and in the lamella (~0.7–2.9 µm) showed significant GC effects of mDia1 on F-actin recruitment (Figure 5D). For the entire cell population (n = 14), the analysis determined causal influence of mDia1 on F-actin assembly at the lamellipodia base and lamella (~0.7–2.9 µm, rank test $P < 0.012$, Figure 5E), but not at the lamellipodia front (0–0.7 µm, rank test $P = 0.452$). The observed G-causal feedback between F-actin on mDia1 (rank test $P < 0.010$, Figure 5E), may represent mDia1's activity to recruit profilin-bound actin for F-actin nucleation and elongation. Overall, the G-causal interaction of mDia1 with F-actin together with the maximal recruitment of mDia1 during retraction events (Figure S4E) indicates that mDia1 initiates actin assembly before protrusion events at the lamellipodia base and in the lamella, in line with our previous observation (13).

Intriguingly, our analysis further revealed a direct G-causal relation between mDia1 and edge velocity at the cell edge, where mDia1 is not G-causal for F-actin assembly (0–0.7 µm, rank test P = 0.008 and P = 0.452, respectively, Figure 5E). This suggests that mDia1 performs an actin-independent function related to edge dynamics and that mDia1's function as an actin elongator is irrelevant at the lamellipodia front. We conjecture that mDia1's actin-independent function in causing edge motion relates to uncapping activities of barbed-end capping proteins (40) or its role in regulating microtubules and cell-matrix adhesions (41, 42).

In summary, these GC analyses unveil a dual role of mDia1 in distinct spatial locations, one as a direct F-actin assembly factor at the base of the lamellipodia, and another as an indirect modulator of edge motion through actin-independent functions.

GC analysis detects causal shifts between wild-type and mutant of VASP deficient in actin assembly

Lamellipodial and lamellar F-actin assembly is regulated by numerous additional factors that are fine-tuning edge motion. In particular, the elongation factor Ena/VASP localizes to the tip of lamellipodia and accelerates elongation of actin filaments (43). We took advantage of the vast biochemical knowledge of VASP-actin interactions to test whether our GC analysis has the sensitivity to detect subtle shifts in F-actin assembly and cell edge movement as a consequence of genetic mutations in VASP.

We co-imaged actin with SNAP-tagged wild-type VASP ($VASP^{WT}$) and Halo-tagged S239D/T278E mutant VASP ($VASP^{MT}$) in a cell line with endogenous VASP knocked down (Figure S6A). In previous work the $VASP^{MT}$ has been described to maintain proper membrane localization, however with attenuated actin polymerization activity (44). In our U2OS cells, $VASP^{WT}$ localized to a narrow band of enrichment at the very tip of the lamellipodia (Figure 6A, Video S15). At large, this localization pattern applied also to $VASP^{MT}$. In detail, the merged images indicated a subtle yet systematic positional shift of $VASP^{WT}$ towards the tip of the cell edge (Figure 6A). By CC analysis, we found that fluctuations in $VASP^{WT}$ recruitment preceded edge protrusions by ~3 s at the very front but were decoupled from edge motion in layers 2-4 (Figure 6B, only layers 1 and 2 are shown). The same spatiotemporal pattern arose for $VASP^{MT}$ recruitment (Figure 6B), although the CC peak in layer 1 was reduced compared to $VASP^{WT}$.

In stark contrast, GC analysis identified marked differences between $VASP^{WT}$ and $VASP^{MT}$. Shown for a representative cell, $VASP^{WT}$ recruitment G-causes actin assembly in most windows at the lamellipodia front (Figure 6C, median P-value 0.047) whereas $VASP^{MT}$ recruitment was non-causal in most windows (median P-value 0.152). The differences were consistent over a cell population sampled over multiple independent experimental sessions (n = 18). $VASP^{WT}$ was G-causal for F-actin assembly at the lamellipodia front (rank test P = 0.025) but not $VASP^{MT}$ (rank test P = 0.831, Figure 6D). This result shows the exquisite sensitivity of GC analysis in pinpointing functional differences in molecular activities that are not detectable merely by CC analysis.

Unexpectedly, GC analysis also indicated a direct causal relation from $VASP^{WT}$ to edge velocity, which was independent of the measured F-actin dynamics (rank test P < 0.001, Figure 6D). $VASP^{MT}$ did not show this direct causal link (rank test P = 0.831, Figure 6D), showing that the significant correlation between $VASP^{MT}$ and edge velocity in Figure 6B does not imply causation.

Next, we used GC analysis to test possible feedback from F-actin to VASP recruitment (Figure 6E). Contrary to the feedback between F-actin and Arp2/3, which accompanies dendritic nucleation of actin filaments throughout the entire lamellipodia, VASP and actin are in bidirectional GC relations only in the most distal layer of the lamella (~2.3–2.9 µm, Figure 6F). We suspect that this relation is a numerical artifact of the strong colocalization of VASP and F-actin at focal adhesions (45) (Video S15), which are stationary with respect to the substrate and thus not properly tracked by subcellular windows following the cell edge.

In summary, co-imaging of $VASP^{WT}$ and $VASP^{MT}$ first confirmed the biochemically characterized deficiency of VASP's S239D/T278E mutation in F-actin assembly in a living cell, second it corroborated the sensitivity of GC-analysis to distinguish correlation from causation, and finally it unveiled direct causal influence of VASP on edge motion. Notably, per our GC-analysis, VASP-elongation of F-actin was confined to the lamellipodia front, without any feedback from F-actin assembly.

Two discrete actin networks independently drive edge motion

Our GC pipeline has thus far delineated spatial zones in which Arp2/3, mDia1, and VASP assume differential roles in assembling F-actin. We wondered whether these three actin regulators operate in parallel

or whether they are causally related among themselves. Specifically, we asked whether Arp2/3 and VASP operate cooperatively, i.e. VASP elongates F-actin filaments that are nucleated by Arp2/3, or separately in differentially regulated F-actin networks (35, 46). In the cooperative case, Arp2/3 recruitment would be expected as indispensable for explaining VASP recruitment. VASP-mediated F-actin assembly may also promote Arp2/3 recruitment, which would be reflected by a G-causal relation from VASP to Arp2/3. Alternatively, if Arp2/3 and VASP operate separately, our pipeline would be expected to report no G-causal relations.

To test these hypotheses, we co-imaged U2OS cells (n = 18) expressing SNAP-tagged exogenous VASP and endogenous Halo-tagged Arp3 (Figure 7A). For a representative cell, the GC tests at individual target windows at the lamellipodia front indicated that neither one of the two actin regulators are causal for the other (Figure 7B, median P-values > 0.222). The absence of such relations was further confirmed at the level of the entire cell population for lamellipodia and lamella (Figure 7C, rank test $P > 0.204$). Furthermore, like with the causal analysis of the relations between Arp2/3, actin, and edge velocity earlier, Arp2/3 and motion remained in a feedback relation regardless of VASP (Figure 7C). On the other hand, VASP is identified as G-causal for edge motion, independent of Arp2/3 (Figure 7C, rank test $P < 0.016$), suggesting that Arp2/3 and VASP function in at least two distinct classes of F-actin architectures, which synergistically drive cell edge protrusion. In line with this prediction, GC pathway analysis indicated that Arp2/3 and VASP contribute as separate F-actin assembling entities to cell edge protrusion (Figure 7D). Of note, the fluctuation signals of Arp2/3 and VASP correlated strongly with zero-time lag, which relates to their concurrent recruitment during P/R cycles (Figure S6D). However, co-recruitment does not mean coupled function in this case. This underlines again the marked difference between correlation and causation analysis.

Discussion

When perturbed, nonlinear regulatory pathways containing feedbacks and redundancies among components tend to respond with instantaneous adaptation, the outcome of which is difficult to interpret and often ambiguous in terms of the immediate function the targeted component assumes in the unperturbed pathway. To reconstruct cause-effect relations in pathways of this characteristic, we adopt here the framework

of Granger causality to infer functional interactions between pathways components from live cell fluorescence imaging of the unperturbed system.

Our pipeline distinguishes with high sensitivity and specificity causation from correlation, and allows the unmixing of functionally distinct molecular activities, which visually seem to be represented by identical fluorescence image fluctuations. This unique feature of the pipeline is illustrated with a VASP mutant that is deficient in actin-polymerization but localizes qualitatively identically to wildtype VASP at the lamellipodia edge. Our analysis confirms that the VASP mutant is not G-causal for F-actin assembly and edge motion, although its recruitment to the leading edge positively correlates with edge motion. Moreover, our analyses reveal that different actin regulators cause F-actin assembly in distinct spatial domains within the lamellipodia and lamella. Arp2/3 is shown to be G-causal for F-actin assembly only in the lamellipodia (0–1.4 µm from the edge), VASP only in the lamellipodia front (0–0.7 µm), and mDia1 at the lamellipodia base and in the lamella (0.7–2.9 µm, Figure S7A).

The Arp2/3 complex requires a pre-formed filament or “mother filament” to act as an actin branch nucleator (47). The origin and source of the mother filament remains obscure. In two independent studies, we have previously suggested that the formin family member mDia1 stimulates Arp2/3 activity *in vitro* and that mDia1 recruitment precedes lamellipodia protrusion onset *in vivo* (13, 38). Our present data in U2OS cells shows that mDia1 initiates actin assembly during retraction and is G-causal for F-actin at the lamellipodia base and in the lamella (Figure 5F). Indeed, this may be the region where mother filament seeds form prior to protrusion onset, followed by autocatalytic nucleation of branched actin after activation and recruitment of Arp2/3 more proximal to the leading edge. In addition to mDia1’s selective G-causal relation for F-actin assembly at the lamellipodia-to-lamella transition, we found a G-causal relationship directly between mDia1 and edge motion at the lamellipodia front, where this nucleator is not G-causal for F-actin. We propose that this actin-independent causality for edge movement relates to mDia1’s function in freeing F-actin barbed ends from capping proteins. This result indicates the unique opportunities perturbation-free analyses generate to distinguish multi-functional properties of components. No perturbation experiment could be designed to determine this duality in mDia1 action in lamellipodia and lamella.

The proposed pipeline for causal inference further identified a direct causal chain at the lamellipodia front from Arp2/3 to F-actin to edge velocity with a feedback from F-actin to Arp2/3 and a chain from VASP to F-actin to edge velocity with an F-actin-polymerization independent GC relation from VASP to edge velocity (Figure S7B). Contrary to the mDia1 scenario (Figure 5F), the causal link from VASP to edge velocity is paralleled by a causal link from VASP to F-actin (Figure 6F), suggesting that the GC pipeline is capturing an additional actin-related yet F-actin-polymerization independent role of VASP relative to cell edge motion.

We interpret this result with a model, in which the membrane-tethered VASP bundles F-actin (either by VASP alone or in cooperation with fascin) (46, 48-50) and thus contributes to protrusion forces in parallel to VASP's activity as an actin polymerase. Indeed, the direct link to edge motion is abrogated by the mutant VASP that also abrogates F-actin bundling (51) (Figures 6D and S6C).

This model is also consistent with our finding that VASP- and Arp2/3-induced F-actin assembly G-causes edge motion independently from each other (Figure 7D), and highlights the sensitivity of our pipeline in deconvolving the inputs of distinct system components into a common effector – information that would have been inaccessible using traditional perturbation approaches.

The key limitation of the GC framework is that G-causal relations can only be determined within the system of co-observed variables (24). While the proposed pipeline determines cause-and-effect relations between pairs of molecular processes, it is not yet able to map out directly causal interactions in larger process circuits with multiple components funneling information through one common component. Remedy to this limitation will arise from the development of hyperspectral imaging of an increasing number of components (52) and from expanded multivariate GC models that integrate data from several rounds of experiments under identical conditions but different configurations of component labeling.

Supplemental information

Methods

Supplemental References

Supplemental Figures S1-S7

Supplemental Videos S1-S15

Acknowledgments

We thank Dr. Dick McIntosh (University of Colorado, Boulder, CO) for kindly providing the U2OS osteosarcoma cells, Dr. Tilmann Bürckstümmer and all Addgene depositors for sharing reagents and Dr. Dana Reed (UT Southwestern Medical Center) for her logistical support and laboratory management. We also thank the UT Southwestern BioHPC facility for providing high-performance computing systems. This study was supported by NIH grants K25EB028854 to JN and R35GM136428 to GD.

Author contributions

Conceptualization: G.D; Methodology: J.N., T.I.; Formal analysis: J.N., T.I., Data Curation: J.N.; Validation: T.I., J.C., K.B.; Resources: T.I., J.C., K.B.; Investigation: G.D., T.I., J.N.; Supervision: G.D.; Funding acquisition: J.N., G.D.; Writing – original draft: J.N., T.I., G.D.; writing – review & editing: J.N., T.I., K.B., G.D.

Declaration of interests

The authors declare no competing interests.

References

1. Vilela M, Danuser G. What's wrong with correlative experiments? Nat Cell Biol. 2011;13(9):1011.
2. Welf ES, Danuser G. Using fluctuation analysis to establish causal relations between cellular events without experimental perturbation. Biophys J. 2014;107(11):2492-8.
3. Hoeller O, Gong D, Weiner OD. How to understand and outwit adaptation. Dev Cell. 2014;28(6):607-16.
4. Insall RH, Machesky LM. Actin dynamics at the leading edge: from simple machinery to complex networks. Dev Cell. 2009;17(3):310-22.
5. Isogai T, Danuser G. Discovery of functional interactions among actin regulators by analysis of image fluctuations in an unperturbed motile cell system. Philos Trans R Soc Lond B Biol Sci. 2018;373(1747).

6. Innocenti M. New insights into the formation and the function of lamellipodia and ruffles in mesenchymal cell migration. Cell Adh Migr. 2018;12(5):401-16.
7. Krause M, Gautreau A. Steering cell migration: lamellipodium dynamics and the regulation of directional persistence. Nat Rev Mol Cell Biol. 2014;15(9):577-90.
8. Blanchoin L, Boujemaa-Paterski R, Sykes C, Plastino J. Actin dynamics, architecture, and mechanics in cell motility. Physiol Rev. 2014;94(1):235-63.
9. Pollard TD. Actin and Actin-Binding Proteins. Cold Spring Harb Perspect Biol. 2016;8(8).
10. Mueller J, Szep G, Nemethova M, de Vries I, Lieber AD, Winkler C, et al. Load Adaptation of Lamellipodial Actin Networks. Cell. 2017;171(1):188-200 e16.
11. Bisaria A, Hayer A, Garbett D, Cohen D, Meyer T. Membrane-proximal F-actin restricts local membrane protrusions and directs cell migration. Science. 2020;368(6496):1205-10.
12. Barnhart EL, Allard J, Lou SS, Theriot JA, Mogilner A. Adhesion-Dependent Wave Generation in Crawling Cells. Curr Biol. 2017;27(1):27-38.
13. Lee K, Elliott HL, Oak Y, Zee CT, Groisman A, Tytell JD, et al. Functional hierarchy of redundant actin assembly factors revealed by fine-grained registration of intrinsic image fluctuations. Cell Syst. 2015;1(1):37-50.
14. Ji L, Lim J, Danuser G. Fluctuations of intracellular forces during cell protrusion. Nat Cell Biol. 2008;10(12):1393-400.
15. Ponti A, Machacek M, Gupton SL, Waterman-Storer CM, Danuser G. Two distinct actin networks drive the protrusion of migrating cells. Science. 2004;305(5691):1782-6.
16. Mendoza MC, Vilela M, Juarez JE, Blenis J, Danuser G. ERK reinforces actin polymerization to power persistent edge protrusion during motility. Sci Signal. 2015;8(377):ra47.
17. Wang C, Choi HJ, Kim SJ, Desai A, Lee N, Kim D, et al. Deconvolution of subcellular protrusion heterogeneity and the underlying actin regulator dynamics from live cell imaging. Nat Commun. 2018;9(1):1688.
18. Machacek M, Hodgson L, Welch C, Elliott H, Pertz O, Nalbant P, et al. Coordination of Rho GTPase activities during cell protrusion. Nature. 2009;461(7260):99-103.
19. Azoitei ML, Noh J, Marston DJ, Roudot P, Marshall CB, Daugird TA, et al. Spatiotemporal dynamics of GEF-H1 activation controlled by microtubule- and Src-mediated pathways. J Cell Biol. 2019;218(9):3077-97.
20. Yang HW, Collins SR, Meyer T. Locally excitable Cdc42 signals steer cells during chemotaxis. Nat Cell Biol. 2016;18(2):191-201.
21. Marston DJ, Vilela M, Huh J, Ren J, Azoitei ML, Glekas G, et al. Multiplexed GTPase and GEF biosensor imaging enables network connectivity analysis. Nat Chem Biol. 2020;16(8):826-33.
22. Granger C. Investigating Causal Relations by Econometric Models and Cross-Spectral Methods. Econometrica. 1969;37(3):424-38.
23. Bressler SL, Seth AK. Wiener-Granger causality: a well established methodology. Neuroimage. 2011;58(2):323-9.
24. Eichler M. Causal inference with multiple time series: principles and problems. Philos Trans A Math Phys Eng Sci. 2013;371(1997):20110613.
25. Eichler M. Granger causality and path diagrams for multivariate time series. J Econometrics. 2007;137(2):334-53.
26. Danuser G, Waterman-Storer CM. Quantitative fluorescent speckle microscopy of cytoskeleton dynamics. Annu Rev Biophys Biomol Struct. 2006;35:361-87.
27. Ma X, Dagliyan O, Hahn KM, Danuser G. Profiling cellular morphodynamics by spatiotemporal spectrum decomposition. PLoS Comput Biol. 2018;14(8):e1006321.
28. Sugiyama K, Tagawa S, Toda M. Methods for Visual Understanding of Hierarchical System Structures. Ieee T Syst Man Cyb. 1981;11(2):109-25.
29. Mogilner A, Oster G. Cell motility driven by actin polymerization. Biophys J. 1996;71(6):3030-45.
30. Higashida C, Kiuchi T, Akiba Y, Mizuno H, Maruoka M, Narumiya S, et al. F- and G-actin homeostasis regulates mechanosensitive actin nucleation by formins. Nat Cell Biol. 2013;15(4):395-405.
31. Batchelder EL, Hollopeter G, Campillo C, Mezanges X, Jorgensen EM, Nassoy P, et al. Membrane tension regulates motility by controlling lamellipodium organization. Proc Natl Acad Sci U S A. 2011;108(28):11429-34.
32. Bieling P, Li TD, Weichsel J, McGorty R, Jreij P, Huang B, et al. Force Feedback Controls Motor Activity and Mechanical Properties of Self-Assembling Branched Actin Networks. Cell. 2016;164(1-2):115-27.

33. Lou HY, Zhao W, Li X, Duan L, Powers A, Akamatsu M, et al. Membrane curvature underlies actin reorganization in response to nanoscale surface topography. Proc Natl Acad Sci U S A. 2019;116(46):23143-51.
34. Risca VI, Wang EB, Chaudhuri O, Chia JJ, Geissler PL, Fletcher DA. Actin filament curvature biases branching direction. Proc Natl Acad Sci U S A. 2012;109(8):2913-8.
35. Pollard TD, Borisy GG. Cellular motility driven by assembly and disassembly of actin filaments. Cell. 2003;112(4):453-65.
36. Blanchoin L, Pollard TD, Mullins RD. Interactions of ADF/cofilin, Arp2/3 complex, capping protein and profilin in remodeling of branched actin filament networks. Curr Biol. 2000;10(20):1273-82.
37. Carlsson AE. Growth velocities of branched actin networks. Biophys J. 2003;84(5):2907-18.
38. Isogai T, van der Kammen R, Leyton-Puig D, Kedziora KM, Jalink K, Innocenti M. Initiation of lamellipodia and ruffles involves cooperation between mDia1 and the Arp2/3 complex. J Cell Sci. 2015;128(20):3796-810.
39. Kamiyama D, Sekine S, Barsi-Rhyne B, Hu J, Chen B, Gilbert LA, et al. Versatile protein tagging in cells with split fluorescent protein. Nat Commun. 2016;7:11046.
40. Shekhar S, Kerleau M, Kuhn S, Pernier J, Romet-Lemonne G, Jegou A, et al. Formin and capping protein together embrace the actin filament in a menage a trois. Nat Commun. 2015;6:8730.
41. Ishizaki T, Morishima Y, Okamoto M, Furuyashiki T, Kato T, Narumiya S. Coordination of microtubules and the actin cytoskeleton by the Rho effector mDia1. Nat Cell Biol. 2001;3(1):8-14.
42. Yamana N, Arakawa Y, Nishino T, Kurokawa K, Tanji M, Itoh RE, et al. The Rho-mDia1 pathway regulates cell polarity and focal adhesion turnover in migrating cells through mobilizing Apc and c-Src. Mol Cell Biol. 2006;26(18):6844-58.
43. Bear JE, Gertler FB. Ena/VASP: towards resolving a pointed controversy at the barbed end. J Cell Sci. 2009;122(Pt 12):1947-53.
44. Benz PM, Blume C, Seifert S, Wilhelm S, Waschke J, Schuh K, et al. Differential VASP phosphorylation controls remodeling of the actin cytoskeleton. J Cell Sci. 2009;122(Pt 21):3954-65.
45. Krause M, Dent EW, Bear JE, Loureiro JJ, Gertler FB. Ena/VASP proteins: regulators of the actin cytoskeleton and cell migration. Annu Rev Cell Dev Biol. 2003;19:541-64.
46. Winkelman JD, Bilancia CG, Peifer M, Kovar DR. Ena/VASP Enabled is a highly processive actin polymerase tailored to self-assemble parallel-bundled F-actin networks with Fascin. Proc Natl Acad Sci U S A. 2014;111(11):4121-6.
47. Mullins RD, Heuser JA, Pollard TD. The interaction of Arp2/3 complex with actin: nucleation, high affinity pointed end capping, and formation of branching networks of filaments. Proc Natl Acad Sci U S A. 1998;95(11):6181-6.
48. Bachmann C, Fischer L, Walter U, Reinhard M. The EVH2 domain of the vasodilator-stimulated phosphoprotein mediates tetramerization, F-actin binding, and actin bundle formation. J Biol Chem. 1999;274(33):23549-57.
49. Breitsprecher D, Kiesewetter AK, Linkner J, Urbanke C, Resch GP, Small JV, et al. Clustering of VASP actively drives processive, WH2 domain-mediated actin filament elongation. EMBO J. 2008;27(22):2943-54.
50. Schirenbeck A, Arasada R, Bretschneider T, Stradal TE, Schleicher M, Faix J. The bundling activity of vasodilator-stimulated phosphoprotein is required for filopodium formation. Proc Natl Acad Sci U S A. 2006;103(20):7694-9.
51. Doppler H, Storz P. Regulation of VASP by phosphorylation: consequences for cell migration. Cell Adh Migr. 2013;7(6):482-6.
52. Valm AM, Cohen S, Legant WR, Melunis J, Hershberg U, Wait E, et al. Applying systems-level spectral imaging and analysis to reveal the organelle interactome. Nature. 2017;546(7656):162-7.

FIGURE LEGENDS

Figure 1. Granger-causality framework to probe functional relations in complex molecular systems

(A) Representation of the complex regulatory circuits integrating cell-intrinsic biochemical and -extrinsic mechanical and chemical cues in the regulation of lamellipodial dynamics (B) Granger-causality analysis is a statistical test that distinguishes causation from correlation. (C-E) Examples of nonlinear regulatory motifs between molecular processes including (C) feedback, (D) redundant pathways, and (E) nested feedbacks. (F-G) Interpretation of Granger-causality in the presence of unobserved latent factors.

Figure 2. Workflow of Granger-causal pathway inference in the study of lamellipodial actin dynamics

(i) Time-lapse fluorescence images of molecules of interest serve as input to infer Granger-causal relations among the molecular processes. (ii) Computer vision algorithms track cell boundaries and probing windows over time to extract cell edge protrusion/retraction velocities and spatiotemporal recruitments of the molecules. (iii) Spatiotemporal fluctuation maps of Arp2/3 (left) and actin (middle) at ~0–0.7 μm from the edge and cell edge velocities (right). (iv) A Granger-causality (GC) test determines whether the Arp2/3 recruitment profile is indispensable for predicting the F-actin assembly in the same probing window. (v) P-values of the GC tests in individual windows provide subcellular evidence of the causal link from Arp2/3 recruitment to F-actin assembly. (vi) The subcellular GC P-values from multiple independent cells are integrated into per-cell median P-values to further test whether causal evidence consistently appears over multiple cells. (vii) The determined Granger-causal relations are represented as graphs, drawn separately for probing window layers at increasing distances from the edge.

Figure 3. Actin and Arp2/3 intensity fluctuations correlate with edge motion

(A) Auto-correlation functions (ACFs) of edge velocity and the recruitment of actin and Arp2/3 in the band ~0–0.7 μm from the edge. Black curves are per-cell averaged ACFs (n = 10 cells), and red curves display their averages. (B-C) Spatiotemporal maps of low-frequency (LF) fluctuations (B) and low-frequency subtracted (LFS) fluctuations (C) of actin assembly in the band ~0–0.7 μm. (D-E) LF fluctuations (D) and LFS fluctuations (E) of Arp2/3 recruitment in the band ~0–0.7 μm. (F-G) ACFs of LFS-recruitment of actin (F) and Arp2/3 (G) in the band ~0–0.7 μm. Black curves are per-cell averaged ACFs (n = 10), and red curves display their averages. (H-I) Cross-correlations of LFS-actin (H) and LFS-Arp2/3 (I) with the edge velocity in individual windows within lamellipodia and lamella for a representative cell. (J-K) Per-cell averaged cross-correlation curves (n = 20, black) of LFS-actin (J) and LFS-Arp2/3 (K) with the edge velocity. Red curves display their averages. Cell-to-cell variability is shown by ±2 × SEM (shaded red bands).

Figure 4. Granger-causality analysis establishes a causal chain from Arp2/3 to F-actin to edge motion

(A-B) Spatial propagation patterns of molecular activities are annotated on a single time point image of a U2OS cell co-expressing mNeonGreen-tagged actin (A) and cytoplasmic HaloTag (B). Magenta windows (left panel) indicate the subcellular regions where molecular fluctuations propagate to four adjacent windows. Arrows (right panel) separately display the spatial propagation in the four different directions. Scale bars, 5 μm. (C) Arp2/3 and actin activity maps and the associated P-values of the GC from Arp2/3 to actin in individual windows for a representative cell. White regions in the map for ~1.4–2.2 μm indicate the absence of corresponding probing windows due to cell morphology. Red indicates significant P-values. (D) The GC from actin to the edge velocity represented as described in (C). (E) Boxplots of per-cell median P-values (n = 20) for six directional Granger-

causal relations between Arp2/3, actin and edge velocity at different distances from the cell edge. The symbol (*) indicates that the per-cell median P-values are significantly smaller than the nominal level 0.05 (Wilcoxon signed rank test).

Figure 5. mDia1 possesses spatially segregated actin polymerization-dependent and polymerization-independent functions in the lamellipodia

(A) Characterization of cells expressing exogenous SNAP-tagged mDia1 (left panel) and endogenously labeled mNG_{11}-mDia1 (right panel). (B) Comparison of molecular sizes of the tagged mDia1s drawn to scale. (C) Representative image of SNAP-actin and endogenously labeled mNeonGreen2-mDia1 observed in a cell. Scale bars, 5 μm. (D) mDia1 and actin activity maps and their associated P-values of the GC from mDia1 to actin in the lamellipodia back (left panel) and lamellipodia-to-lamella transition area (right panel) from the cell shown in (C). Red indicates significant P-values. (E) Boxplots of per-cell median P-values (n = 14) of Granger-causal relations between mDia1, actin and edge velocity. The symbol (*) indicates that the per-cell P-values are significantly smaller than 0.05 (Wilcoxon signed rank test). (F) GC pathway diagrams between mDia1, actin and edge velocity in the lamellipodia and lamella regions.

Figure 6. Granger-causality analysis distinguishes mutant phenotypes from wild-type VASP recruitment profiles co-imaged within the same cells

(A) Representative images of a U2OS cell (left) co-expressing mNeonGreen-actin, SNAP-tagged wild-type VASP ($VASP^{WT}$) and Halo-tagged S239D/T278E VASP mutant ($VASP^{MT}$). Scale bars, 5 μm. The insets are enlarged in the right panel. (B) Per-cell averaged cross-correlation curves (n = 18, black) of $VASP^{WT}$ (left) and $VASP^{MT}$ (right) with the edge velocity. Red curves display their averages. Cell-to-cell variability is shown by ±2 × SEM (shaded red bands). (C) Activity maps of actin, $VASP^{WT}$ (left) and $VASP^{MT}$ (right), and the associated P-values of the GC from $VASP^{WT}$ and $VASP^{MT}$ to actin in the lamellipodia front from the cell shown in (A). Red indicates significant P-values. (D) Boxplots of per-cell median P-values (n = 18) of Granger-causal relations for $VASP^{WT}$ (left) and $VASP^{MT}$ (right). The symbol (*) indicates that the per-cell P-values are significantly smaller than 0.05 (Wilcoxon signed rank test). (E) Granger-causal relations among $VASP^{WT}$, actin and edge velocity as described in (D). (F) GC pathway diagrams between $VASP^{WT}$, actin and edge velocity in the lamellipodia and lamella regions.

Figure 7. Two discrete F-actin networks drive edge motion

(A) A single time point image of a U2OS cell co-expressing endogenously Halo-tagged Arp3 and exogenous SNAP-tagged VASP. Scale bars, 5 μm. (B) Arp2/3 (1^{st} panel) and VASP (2^{nd} panel) activities at the lamellipodia front from the cell shown in (A). Associated P-values of the GC from Arp2/3 to VASP (3^{rd} panel) and from VASP to Arp2/3 (4^{th} panel) in individual windows. Red indicates significant P-values. (C) Boxplots of per-cell median P-values (n = 18) of Granger-causal relations between Arp2/3, VASP and edge velocity at different distances from the cell edge. The symbol (*) indicates that the per-cell P-values are significantly smaller than 0.05 (Wilcoxon signed rank test). (D) GC pathway diagrams between Arp2/3, VASP and edge velocity in the lamellipodia and lamella regions.

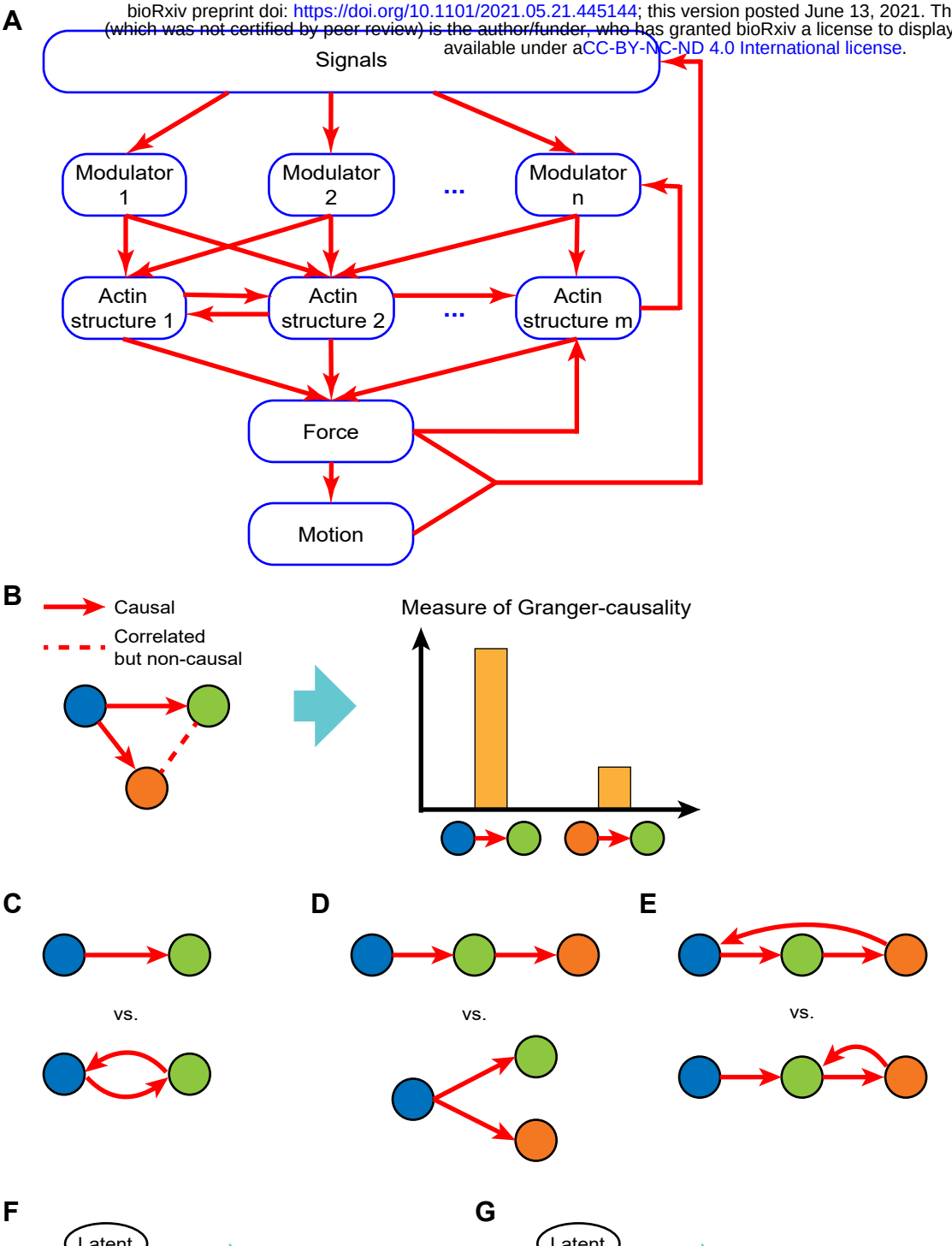

(i) Live cell fluorescence movies

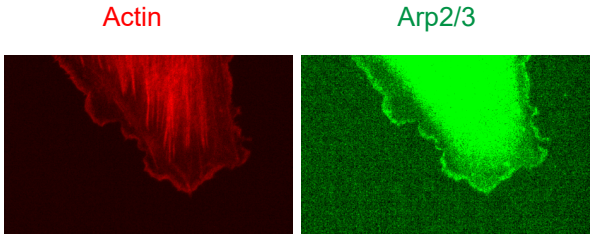

(ii) Tracking morphodynamic/molecular activities

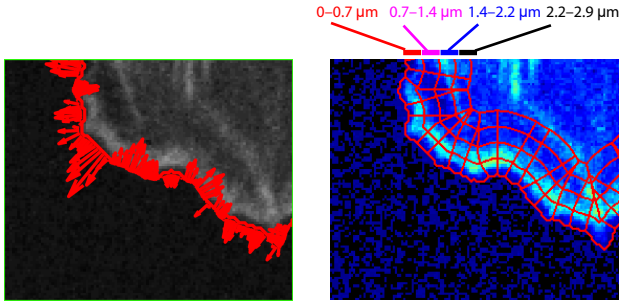

(iii) Readouts of subcellular activities

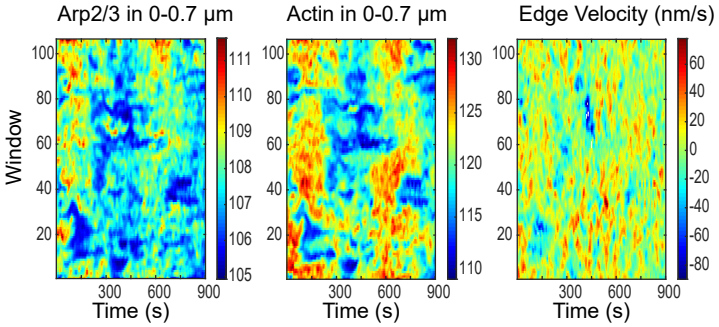

(iv) Granger-causality (GC) test at a single window

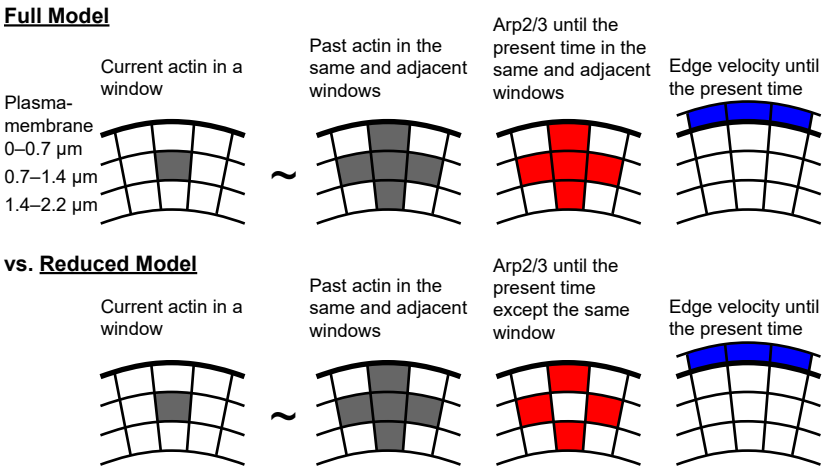

If **Full Model » Reduced Model**, Arp2/3 ⟶ Actin in the window.

(v) Subcellular causal evidences for one cell

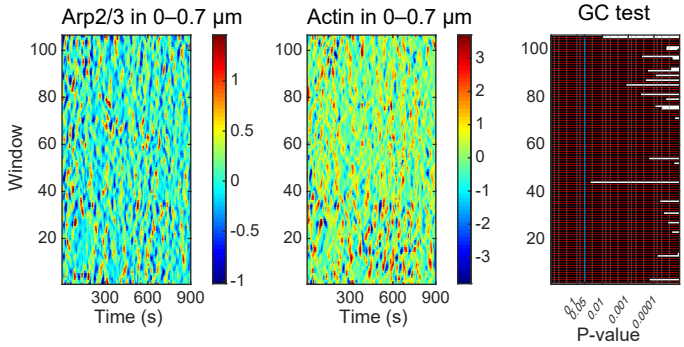

(vi) Granger-causal evidences for multiple cells

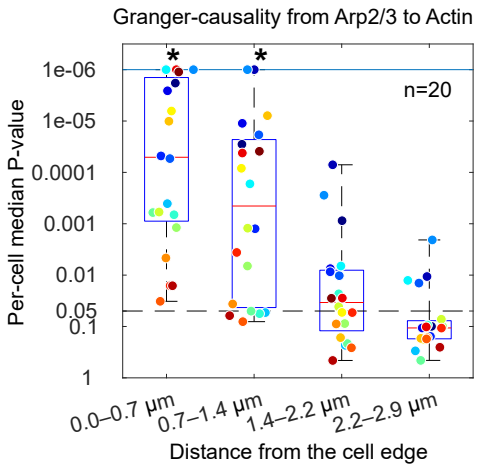

(vii) Granger-causal pathway diagram